JSML
Journal of Science and Mathematics Letters
ISSN 2462-2052 • eISSN 2600-8718

Research Article

Isolation of Phytochemicals from *Calophyllum nodosum* and In Silico Evaluation of Their Drug-Likeness and DNA Gyrase Inhibition Potential

Yiizamy Suffian[1], Vivien Jong Yi Mian[2], Ainaa Nadiah Abd Halim[1], Jiumn-Yih Wu[3], Wafa M. Al Madhagi[4], Nor Hisam Zamakshshari[1*]

[1] Faculty of Resource Science and Technology, Universiti Malaysia Sarawak, 94300 Kota Samarahan, Sarawak, Malaysia
[2] Faculty of Applied Science Studies, Universiti Teknologi MARA, 94300 Kota Samarahan, Sarawak, Malaysia
[3] Department of Food Science, National Quemoy University, Kinmen, 890301, Taiwan
[4] Department of Pharmaceutical Chemistry, Faculty of Pharmacy, Sana'a University, 31220 Sana'a, Yemen
* Corresponding author: znhisam@unimas.my

ARTICLE HISTORY

Received
24 July 2025
Revised
30 September 2025
Accepted
6 October 2025
Published
2 January 2026

KEYWORDS

ADME
Antibacterial
Calophyllum nodosum
DNA gyrase
Molecular docking
Phytoconstituents

ABSTRACT

The *Calophyllum* species have gained a lot of attention for their structurally diverse secondary metabolites with potential biological activities, including antibacterial scaffolds. A detailed study done on the phytochemical profile of the *Calophyllum nodosum* stem bark has led to the isolation of three xanthones, trapezifolixanthone (**1**), caloxanthone C (**2**), 1-hydroxy-7-methoxyxanthone (**3**), and a cyclic ester, canumolactone (**4**). Their structures were characterised using spectroscopic techniques like NMR, MS, and IR, and the spectra were confirmed with the previous literature. The pharmacokinetic properties of the compounds were predicted using SwissADME and cross-validated using pkCSM, while molecular docking simulation against bacterial DNA gyrase was performed using Autodock Vina. All isolated compounds met the drug-likeness requirements under Lipinski's rule, according to the ADMET predictions, showing favourable oral and gastrointestinal bioavailability and absorption. Canumolactone (**4**), in particular, showed the best combination of solubility, clearance, and the least amount of CYP liabilities. The molecular docking simulation revealed that trapezifolixanthone (**1**) gave the strongest binding affinity to DNA gyrase among all isolated compounds, surpassing the binding affinity of the standard inhibitor, BDBM50198240. The current study presents the first combined ADMET predictions and molecular docking analysis for compounds isolated from *C. nodosum*. The findings provide preliminary evidence of their potential as drug-like scaffolds for future pharmacological development.

https://doi.org/10.37134/jsml.vol14.1.1.2026

1. INTRODUCTION

The role of antimicrobial agents, including antivirals, antibiotics, antifungals, and antiprotozoals, are pivotal in combating diseases. However, the escalating issue of antimicrobial resistance (AMR) poses a threat to global health (Glanzmann et al., 2024). Factors such as the misuse and inadequate control practices of antibiotics have accelerated resistance, leading to previously useful antimicrobial agents now being ineffective (Hong et al., 2024). In 2019, millions of deaths were associated with drug-resistant infections, and this figure could soar to 10 million deaths annually by 2050 if effective interventions are not implemented (Murray et al., 2022), potentially making common infections untreatable (Salam et al., 2023).

Natural products remain a foundation in drug discovery, with a significant percentage of currently approved drugs being derived from plant-based secondary metabolites (Li et al., 2022; Newman & Cragg, 2020). The genus *Calophyllum* (family: Clusiaceae) comprises evergreen broad-leaved trees that are primarily distributed in tropical regions of Southeast Asia, including Malaysia (Zailan et al., 2022). Several species from this genus are widely used in the traditional medicinal system to treat skin infections, wounds, ulcers, and rheumatism (Farida et al., 2024). Numerous investigations into their phytochemical profile have revealed the presence of various classes of secondary metabolites, including xanthones, coumarins, triterpenes, and sterols (Chinthu et al., 2023), which contribute to their ethnomedical applications. These secondary metabolites were reported to exhibit a wide range of biological activities, which include antibacterial (Remali et al., 2022), anticancer (Zailan et al., 2022), anti-inflammatory (Feng et al., 2020), and cytotoxic properties (Zaini et al., 2025). Among the numerous species within this genus is *Calophyllum nodosum*, one of the species that grows abundantly in Malaysia. It is native to tropical regions and remains relatively underexplored compared to its counterparts.

The advancement of computational chemistry enables the rapid in silico evaluation of pharmacokinetic properties and molecular interactions complementing natural product research. Tools such as SwissADME (Daina et al., 2017) and ADMETlab 3.0 (Xiong et al., 2021) provide reliable predictions on absorption, distribution, metabolism, excretion, and toxicity (ADMET), offering an early assessment of the potential drug-likeness for the natural compounds. Furthermore, molecular docking approaches have become indispensable for identifying potential binding modes and affinities of phytochemicals with biologically relevant protein targets (Morris et al., 2009; Trott & Olson, 2010). Collectively, these computational methods accelerate the early phases of drug discovery and provide valuable mechanical insights.

This study reports the isolation of trapezifolixanthone (**1**), caloxanthone C (**2**), 1-hydroxy-7-methoxyxanthone (**3**), and canumolactone (**4**). Their pharmacokinetic profiles were systematically evaluated using ADME prediction platforms, and molecular docking was conducted to evaluate the antibacterial potential of the isolated compounds by targeting DNA gyrase, a crucial enzyme involved in DNA replication for bacteria. This study represents the first in silico characterisation of *C. nodosum* metabolites. The findings provide preliminary evidence for their potential as drug-like molecules and establish a foundation for further pharmacological validation.

2. METHODOLOGY

2.1. Plant Material

The stem bark of *C. nodosum* (Voucher No. UiTM3050) was collected from Gunung Santubong, Kuching, Sarawak, and authenticated at the herbarium, Faculty of Applied Science, Universiti Teknologi Mara (UiTM) Sarawak, Kota Samarahan 2.

2.2. General Experimental Procedures

The extraction, isolation, and purification processes employed analytical grade solvents of *n*-hexane, dichloromethane, chloroform, ethyl acetate, acetone, and methanol. Silica gel Merck 60 (1.07734.1000 and 1.09385.1000) and Sephadex LH-20 (Sigma Aldrich) were used as the stationary phase for column chromatography. TLC was performed on silica gel 60 F254 aluminium sheets, and the radial chromatography plate was prepared using silica gel Merck 60 PF254 (1.07749.1000) with gypsum in 0.5, 1.0, and 2.0 mm thickness. Spots were visualised under UV light (254 and 366 nm). NMR spectra (400 MHz for ^{1}H, 100 MHz for ^{13}C) were recorded on a Bruker spectrometer (Bruker AV400III HD 400 MHz) using $CDCl_3$ and acetone-d_6 as deuterated solvents. IR spectra were obtained via ATR-FTIR (Perkin Elmer Frontier), and MS spectra were obtained on Shimadzu (CBM-20A

spectrometer, GC-MS-QP 5050A spectrometer), while melting points were obtained on a Stuart SMP3 (Keison, United Kingdom).

2.3. Extraction and Isolation

The stem bark of *C. nodosum* (2.68 kg) was air-dried for a few weeks and ground into a fine powder using a laboratory grinder. The powdered stem bark was extracted with *n*-hexane for 72 hours using the cold maceration technique three times. Then, the extract was filtered and concentrated using the rotary evaporator (Heidolph Laborota 4000 efficient) to obtain the crude extract. It was kept under a fume hood and weighed until a constant weight was obtained. The procedure was repeated for chloroform and methanol, sequentially, yielding hexane (229.0 g), chloroform (61.6 g), and methanol (284.0 g) extracts.

The crude extracts obtained from *C. nodosum* stem bark were subjected to multiple chromatographic separations to isolate the secondary metabolites. The hexane extract (229.0 g) was mixed with silica gel using a ratio of 1:1 extract to silica for dry loading. The sample was then subjected to gravity column chromatography with silica gel 60 (230-400 mesh) as the stationary phase and a sequential solvent system of hexane:chloroform, chloroform:ethyl acetate, and ethyl acetate:methanol, affording 19 fractions (CnH1-19). Fractions CnH1-11 were combined and rinsed with methanol to remove the insoluble terpenoid crystals. The methanol-soluble residual (CnH1b) was chromatographed repeatedly on Sephadex LH-20 CC with 100% methanol as the mobile phase to yield 12 fractions (CnH1b3b5e1-12). Fractions 7-12 were loaded to radial chromatography with eluent hexane:acetone (98:2, v/v), resulting in six subfractions (CnH1b3b5e7a-f). The purification of fraction b (hexane:acetone, 98:2, v/v) has led to the identification of compound **2** in fraction 3 and compound **3** in fraction 6.

Fractions CnH17-19 were combined and fractionated on silica CC using hexane:chloroform:acetone gradient systems, yielding subfractions a-do. Subfractions v-ah were further separated using hexane:chloroform:methanol gradients into 33 fractions. The isolation of fractions 4-25 on radial chromatography with chloroform:acetone (99:1, v/v) has yielded fractions a-am. Fractions e-y were then further separated on Sephadex LH-20, giving eight subfractions. From these, fractions 3-8 were further isolated with hexane:chloroform (2:8, v/v), affording fractions a-ac. Subfractions o-q were fractionated with eluent hexane:acetone (8:2, v/v), producing four subfractions. The purification of the second fraction with hexane:dichloromethane (9:1, v/v) has yielded compounds **4** and **3**.

The chloroform extract (61.6 g) was fractionated using a hexane:chloroform:methanol solvent gradient, affording 11 fractions (CnC1-11). Fractions CnC3-7 were combined and separated on Sephadex LH-20 to yield subfractions a-o. Fractions b-f were further subjected to silica CC with hexane:ethyl acetate (96:4, v/v), producing eight fractions. The isolation of subfractions 1-5 with hexane:ethyl acetate (95:5, v/v) using radial chromatography has afforded compound **1**. Meanwhile, fractions 6-7 as subjected to radial chromatography with hexane:acetone (95:5, v/v), affording five fractions (a-e), of which fraction “e” yielded compound **2**. Subfractions c-d were additionally purified using hexane:chloroform (7:3, v/v) to provide another portion of compound **1**.

2.4. ADMET Test

The structures of the isolated compounds (**1**-**4**) were drawn in ChemDraw software 22.0 and converted to Canonical Simplified Molecular Input Line Entry System (SMILES). SwissADME from the Swiss Institute of Bioinformatics and pkCSM from the Biosig Lab, University of Melbourne, were utilised as in silico platforms for ADMET prediction. All predictions were performed on 10 September 2025. SwissADME (http://www.swissadme.ch/) was employed to screen various characteristics of molecules, including their physicochemical traits, pharmacokinetic behaviour, drug-likeness, and compatibility with medicinal chemistry. It is widely used for assessing drug-likeness profiles through parameters such as Lipinski’s rule, which provides a benchmark for identifying compounds with a high probability and oral bioavailability. One of its features is a RADAR plot that visualises key parameters such as saturation, polarity, molecular weight, lipophilicity, and solubility (Daina et al., 2017).

pkCSM (https://biosig.lab.uq.edu.au/pkcsm/prediction) utilises graph-based molecular signatures to forecast and optimise pharmacokinetic properties and toxicity profiles. The platform extends the cut-off scanning matrix (CSM) idea to generate accurate simulations of ADMET characteristics. pkCSM has demonstrated strong predictive performance, with an external validation accuracy of 83.8% for mutagenicity assessment. It provides numerous endpoints, including LD_{50},

Ames mutagenicity, maximum tolerated dose, and hepatotoxicity, making it a valuable complementary tool for in silico drug development after application of SwissADME (Al Azzam, 2023).

2.5. Molecular Docking Simulation

The two-dimensional structures of all isolated compounds **1**-**4** were constructed with Discovery Studio® 4.0 (Accelrys, San Diego, USA) and were exported as a PDB file. Geometric and energy optimisations of the compounds were performed with Avogadro (Hanwell et al., 2012), which applies the MMFF94 force field alongside the steepest descent and conjugate gradient algorithms to ensure optimal conformational stability. The crystal structure of the target macromolecule was retrieved from the Protein Data Bank (https://www.rcsb.org/). This macromolecule was selected based on two criteria: (i) a resolution of less than 3.0 Å, and (ii) the presence of a bound inhibitor within the structure, which facilitated accurate active site identification. The DNA gyrase enzyme (PDB ID: 5L3J) was selected as it satisfied the criteria mentioned. The hydrogen atoms were bound to the protein structure using AutoDockTools to prepare it for docking. Molecular docking simulations were conducted using AutoDock Vina (Eberhardt et al., 2021). A redocking procedure was carried out by reintroducing the native inhibitor into the crystal structure to validate the docking parameters. This step ensured the reproducibility and reliability of the docking results. The top-ranked docking pose was superimposed onto the original crystal structure to verify its alignment within the active site. Ligands were prioritised based on their calculated binding energies, and the compound exhibiting the highest affinity was selected for further investigation. Binding interactions were visualised and analysed using *Discovery Studio® 4.0*, with detailed inspection of the selected ligand's orientation and interaction profile

3. RESULTS AND DISCUSSION

3.1. Isolation of Secondary Metabolites

The further purification of both hexane and chloroform extracts of the stem bark parts of *C. nodosum* using a combination of chromatographic techniques resulted in trapezifolixanthone (**1**) (27.5 mg), caloxanthone C (**2**) (43.6 mg), 1-hydroxy-7-methoxyxanthone (**3**) (22.7 mg), and canumolactone (**4**) (110.8 mg). The structural elucidation of the compounds was achieved through detailed spectroscopic analysis, including 1D and 2D NMR experiments, MS, IR, and comparisons with reported data in the literature (Karunakaran et al., 2022; Lee et al., 2017; Dharmaratne et al., 2009; Lizazman & Jong, 2024). Figure 1 depicts the structures of compounds **1**-**4**, and their respective NMR spectra are retrievable in the supplementary material.

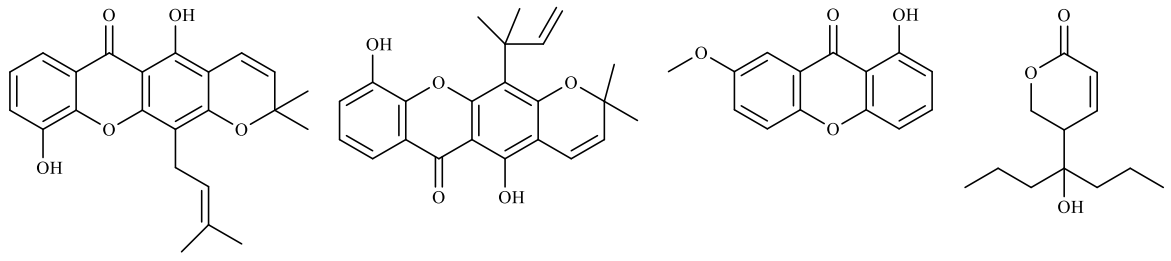

1 **2** **3** **4**

Figure 1. The chemical structures of compounds **1**-**4**.

Compound **1** was obtained as yellow needle-like crystals from both the hexane and chloroform extracts, with a melting point of 160-162°C. The molecular formula $C_{23}H_{22}O_5$ was deduced from the molecular ion peak at *m/z* 378 $[M+H]^+$ in the MS spectrum. The UV spectrum displayed a maximum absorption at 286 nm, indicative of a conjugated xanthone system. The IR spectrum showed characteristic absorptions at 3323 cm^{-1} (OH), 1720 cm^{-1} (C=O), and 1651–1580 cm^{-1} (C=C aromatic), in agreement with typical xanthone scaffolds. The ^1H NMR spectrum exhibited the most shifted singlet peaks, including a chelated hydroxyl proton at δ_H 13.34, a downfield hydroxyl at δ_H 9.24. The indicative of a pyrano ring was observed as two olefinic doublets at δ_H 6.72 and 5.77 (J = 10.0 Hz), and a singlet methyl resonances at δ_H 1.51, integrated for six protons. The prenyl moiety was confirmed by resonances at δ_H 3.57 (H-1″), 5.31 (H-2″), and the two methyls of δ_H 1.66 (H-4″) and δ_H 1.87 (H-5″). The ^{13}C NMR spectrum revealed 23 carbons, including one carbonyl at δ_C 182.2, multiple oxygenated quaternary carbons (δ_C 159.1, 156.6, 154.8, 147.2, 146.4), and prenyl carbons consistent with

literature values. Comparison of all spectral data with published reports confirmed the identity of compound **1** as trapezifolixanthone (Karunakaran et al., 2022).

Compound **2** was isolated as yellow needle-like crystals from the hexane and chloroform extracts as well, with a melting point of 214-215°C. The molecular formula $C_{23}H_{22}O_5$ was supported by the molecular ion peak at *m/z* 378 $[M+H]^+$ in the MS spectrum. The IR spectrum showed absorptions for hydroxyl (3440 cm^{-1}), conjugated carbonyl (1741 cm^{-1}), aromatic C=C (1649 cm^{-1}), and C–O stretching (1218 cm^{-1}), characteristic of xanthone derivatives. The ^{1}H NMR spectrum displayed a chelated hydroxyl proton at δ_H 13.71, a second hydroxyl at δ_H 8.96, and three aromatic protons at δ_H 7.37, 7.28, and 7.66, confirming the xanthone framework. Additional diagnostic signals included *ortho*-coupled olefinic protons at δ_H 6.73 and 5.80 (*J* = 10.0 Hz), and a singlet at δ_H 1.52 (6H, s), consistent with a 2,2-dimethyl-2H-pyrano ring. Signals corresponding to a 1,1-dimethylallyl substituent were also observed (δ_H 1.76, δ_C 41.8, δ_C 152.5), supporting its attachment to C-4 of the xanthone core. The ^{13}C NMR spectrum confirmed 23 carbons, including a carbonyl at δ_C 182.4, oxygenated quaternary carbons, and prenyl carbons in agreement with published data. Taken together, the spectroscopic evidence confirmed the identity of compound **2** as caloxanthone C (Lee et al., 2017).

Compound **3** was obtained as pale-yellow needle-like crystals, discovered from both hexane and chloroform extracts, with a melting point of 121-124°C. The IR spectrum showed absorptions at 3279 cm^{-1} (OH), 1738 cm^{-1} (C=O), 1646 cm^{-1} (C=C aromatic), and 1236 cm^{-1} (C–O), consistent with a xanthone skeleton. The ^{1}H NMR spectrum revealed a chelated hydroxyl proton at δ_H 12.71 and a methoxy singlet at δ_H 3.97 (3H, s, OCH_3), confirming substitution at C-7. Two sets of mutually coupled aromatic protons at δ_H 7.74, 7.04, 6.81 and δ_H 7.64, 7.61, 7.53 established the presence of two distinct aromatic rings within the xanthone scaffold. The ^{13}C NMR spectrum showed 14 carbons, including one carbonyl at δ_C 183.3, six quaternary carbons, six methines, and one methyl, consistent with a methoxy-substituted xanthone. The HMBC correlations further supported the placement of the hydroxyl at C-1 and the methoxy group at C-7. Taken together, these data confirmed the identity of compound **3** as 1-hydroxy-7-methoxyxanthone, consistent with the previously reported value (Dharmaratne et al., 2009).

Compound **4** was obtained as a yellowish-orange oil from the hexane extract of *C. nodosum*. The MS spectrum gave $[M+H]^+$ at *m/z* 212.30, consistent with the $C_{12}H_{20}O_3$ molecular formula. The IR spectrum exhibited absorptions for a lactone carbonyl (1725 cm^{-1}), C=C stretch (<3000 cm^{-1}), and C-O-C stretch (1268 cm^{-1}), confirming an ester within a cyclic system. The ^{1}H NMR spectrum displayed olefinic protons δ_H 7.77 (H-3) and 7.67 (H-4) as doublets of doublets, oxygenated methylene δ_H 4.23 (H-6), a methine at δ_H 1.71 (H-5), aliphatic methylenes δ_H 1.33–1.42, and terminal methyl triplets δ_H 0.92 (H-7′) and 0.95 (H-4′). COSY confirmed connectivity within the lactone ring and side chains. The ^{13}C NMR and DEPT spectra revealed 12 carbons: one carbonyl δ_C 167.1 (C-2), two olefinic δ_C 128.7 (C-3), 131.1 (C-4), an oxygenated methylene δ_C 67.4 (C-6), methylenes δ_C 20–30 ppm, and terminal methyls δ_C 13.4, 10.4. The HSQC data further confirmed the C–H pairs, while HMBC showed H-3 (δ_H 7.77) correlating with C-2 (δ_C 167.1) and C-4 (δ_C 131.1), and H-6 (δ_H 4.23) with C-2 and C-5, proving a closed lactone ring. Correlations among aliphatic protons and carbons indicated two identical alkyl branches attached to the lactone. Based on all the information, compound **4** was identified as canumolactone (Lizazman & Jong, 2024).

3.2. Spectral Data of Compound (1-4)

Trapezifolixanthone (**1**). Yellow needle crystal (27.5 mg). $C_{23}H_{22}O_5$. m.p: 160-162°C (168-169°C, Lizazman et al., 2023). ^{1}H NMR (400 MHz, acetone-d_6) δ H: 13.45 (*s*, 1-OH), 9.21 (*s*, 5-OH), 7.72 (1H, *dd*, *J* = 7.9 Hz, 1.6 Hz, H-8), 7.39 (1H, *dd*, *J* = 7.9 Hz, 1.5 Hz, H-6), 7.31 (1H, *t*, *J* = 7.9 Hz, H-7), 7.09 (1H, *d*, *J* = 10.0 Hz, H-1′), 5.79 (1H, *d*, *J* = 10.0 Hz, H-2′), 5.26 (1H, *t*, *J* = 7.4 Hz, H-2″), 3.36 (2H, *d*, *J* = 7.4 Hz, H-1″), 1.83 (3H, *s*, H-5″), 1.67 (3H, *s*, H-4″), 1.52 (3H, *s*, H-4′), 1.52 (3H, *s*, H-5′). ^{13}C NMR (100 MHz, acetone-d_6) δ C: 182.2 (C-9), 159.2 (C-3), 156.6 (C-1), 154.9 (C-4a), 147.2 (C-5), 146.4 (C-5a), 131.8 (C-3″), 128.7 (C-2′), 124.8 (C-7), 123.3 (C-2″), 122.1 (C-8a), 121.5 (C-6), 116.3 (C-8), 116.0 (C-1′), 108.6 (C-4), 105.1 (C-9a), 104.0 (C-2), 79.1 (C-3′), 28.5 (C-4′), 28.5 (C-5′), 26.0 (C-4″), 22.0 (C-1″), 18.1 (C-5″) (Karunakaran et al., 2022).

Caloxanthone C (**2**). Yellow needle crystal. $C_{23}H_{22}O_5$. m.p: 214-215°C (211-213°C, (Zamakshshari et al., 2016). ^{1}H NMR (400 MHz, acetone-d_6): 13.70 (*s*, 1-OH), 8.95 (*s*, 5-OH), 7.65 (1H, *dd*, *J* = 1.2 Hz, 7.9 Hz, H-8), 7.36 (1H, *dd*, *J* = 1.1 Hz, 7.9 Hz, H-6), 7.26 (1H, *t*, *J* = 7.9 Hz, H-7), 6.72 (1H, *d*, *J* = 10.0 Hz, H-1′), 6.52 (1H, *dd*, *J* = 10.6 Hz, 17.5 Hz, H-2″), 5.74 (1H, *d*, *J* = 10.0 Hz, H-2′), 5.04 (1H, *dd*, *J* = 0.88 Hz, 17.5 Hz, H-3″), 4.88 (1H, *dd*, *J* = 1.0 Hz, 10.6 Hz, H-3″), 1.75 (6H, *s*, H-4″ & H-5″), 1.51 (6H, *s*, H-4′ & H-5′). ^{13}C NMR (100 MHz, acetone-d_6): 181.5 (C-9), 159.3 (C-3),

156.3 (C-1), 155.0 (C-4a), 151.7 (C-2″), 146.4 (C-5), 145.1 (C-5a), 127.7 (C-2′), 124.0 (C-7), 120.1 (C-8a), 120.0 (C-6), 115.4 (C-1'), 115.0 (C-8), 113.5 (C-4), 106.6 (C-3″), 104.9 (C-2), 103.5 (C-9a), 78.4 (C-3′), 40.9 (C-1″), 29.0 (C-4″ & C-5″), 27.2 (C-4′ & C-5′) (Lee et al., 2017).

1-Hydroxy-7-methoxyxanthone (**3**). Pale yellow needle crystal. $C_{14}H_{10}O_4$. m.p: 121-124°C (124-126°C, (Leslie Gunatilaka et al., 1982). ^{1}H NMR (400 MHz, acetone-d_6): 12.71 (*s*, 1-OH), 7.74 (1H, *t*, *J* = 8.4 Hz, H-3), 7.64 (1H, *d*, *J* = 3.1 Hz, H-8), 7.61 (1H, *d*, *J* = 9.2 Hz, H-5), 7.52 (1H, *dd*, *J* = 3.1 Hz, 9.2 Hz, H-6), 7.04 (1H, *dd*, *J* = 1.0 Hz, 8.4 Hz, H-4), 6.81 (1H, *dd*, *J* = 1.0 Hz, 8.2 Hz, H-2), 3.97 (*s*, 7a-OCH3). ^{13}C NMR (100 MHz, acetone-d_6): 182.0 (C-9), 161.8 (C-1), 156.4 (C-7), 154.9 (C-4a), 151.0 (C-5a), 137.0 (C-3), 125.6 (C-6), 120.7 (C-8a), 119.5 (C-5), 109.9 (C-2), 108.3 (C-9a), 107.0 (C-4), 105.1 (C-8), 55.4 (C-7a) (Dharmaratne et al., 2009).

Canumolactone (**4**). Yellowish orange, oily. ^{1}H NMR (400 MHz, acetone-d_6): 7.77 (1H, *dd*, *J* = 3.4 Hz, 5.8 Hz, H-3), 7.67 (1H, *dd*, *J* = 3.4 Hz, 5.8 Hz, H-4), 4.23 (2H, *m*, H-6), 1.72 (1H, *m*, H-5), 1.46 (2H, *m*, H-3′), 1.40 (2H, *m*, H-2′), 1.36 (2H, *m*, H-5′), 1.31 (2H, *m*, H-6′), 0.95 (3H, *t*, *J* = 7.2 Hz, H-4′), 0.92 (3H, *t*, *J* = 7.1, H-7′). ^{13}C NMR (100 MHz, acetone-d_6): 167.1 (C-2), 132.6 (C-1′), 131.1 (C-4), 128.7 (C-3), 67.4 (C-6), 38.8 (C-5), 30.3 (C-2′), 28.8 (C-5′), 23.6 (C-3′), 22.7 (C-6′), 13.4 (C-7′), 10.4 (C-4′) (Lizazman & Jong, 2024).

The structures of the isolated compounds were generated with ChemDraw software 22.0 subsequently converted into canonical SMILES format. The SMILES format of each compound was further confirmed through the PubChem website. Table 1 shows the SMILES code of compounds **1-4** produced from ChemDraw.

Table 1. The SMILES code of all isolated compounds

Compounds	Canonical SMILES
1	CC(=CCC1=C2C(=C(C3=C1OC4=C(C3=O)C=CC=C4O)O)C=CC(O2)(C)C)C
2	OC1=CC=CC2=C1OC3=C(C(O)=C(C=CC(C)(C)O4)C4=C3C(C)(C)C=C)C2=O
3	O=C1C2=C(OC3=C1C=C(OC)C=C3)C=CC=C2O
4	O=C1OCC(C(CCC)(CCC)O)C=C1

3.3. ADME Profiling

3.3.1. SwissADME

The structural features of phytoconstituents in SMILES format were entered into the SwissADME and pkCSM websites. The phytochemicals analysed include compounds (**1-4**) for evaluation of their ADME properties. Figure 2 displays the criteria to be considered as "good", according to Lipinski's Rule of Five (Ranjith & Ravikumar, 2019). All guidelines for prediction models and interpretation of SwissADME results were based on the literature (Daina et al., 2017).

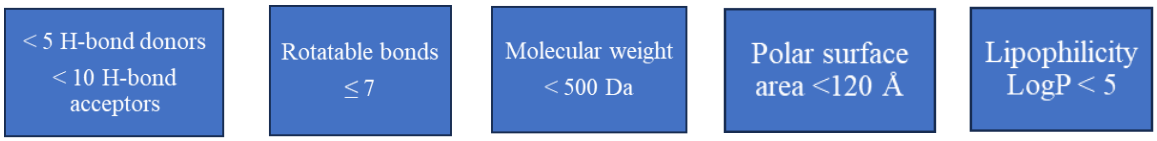

Figure 2. The Lipinski's Rule of Five

Compounds **1** and **2** are both xanthone derivatives with identical molecular weights of 378.42 g/mol, indicating that they share closely related physicochemical parameters, including two hydrogen bond donors, five acceptors, and a TPSA of 79.9 Å², as shown in Table 2. Their consensus LogP values are 4.39 and 4.38, respectively, which indicate that they are moderate in lipophilicity, while water solubility predictions in SwissADME consistently classified compounds **1** and **2** as poorly soluble, with LogS (ESOL) ≈ -6.0. These features are in line with the high aromaticity, planar tricyclic system, and limited polarity of xanthones, which restrict their aqueous solubility and drug-likeness (Kurniawan et al., 2021; Pinto et al., 2021). In contrast, compounds **3** (MW 242.23 g/mol) and **4** (MW 212.29 g/mol) displayed lower lipophilicity with their consensus LogP at 2.50 and 2.14, respectively, as shown in Table 3. The solubility of compound **4** is the best among the isolated compounds, as shown in Table 4 across different models tested. This is supported by their low aromaticity and higher fraction of sp^3 carbons. According to Rai et al. (2023) and Wei et al. (2020), this type of structural feature is generally correlated with improved oral absorption and metabolic stability. This prediction also matched the physical characteristics of compound **4**, as it is isolated in liquid form.

Table 2. Physicochemical properties of the isolated compounds from *C. nodosum*

Compound (MW, g/mol)	Num. heavy atoms	Num. arom. heavy atoms	Fraction Csp3	Num. rotatable bonds	Num. H-bond acceptors	Num. H-bond donors	Molar refractivity	TPSA (Å^2)
1 (378.42)	28	14	0.26	2	5	2	111.88	79.9
2 (378.42)	28	14	0.26	2	5	2	111.76	79.9
3 (242.23)	18	14	0.07	1	4	1	68.51	59.67
4 (212.29)	15	0	0.75	5	3	1	59.69	46.53

TPSA - Topological Polar Surface Area; MW – molecular weight

Table 3. Lipophilic characteristics of the isolated compounds from *C. nodosum*

Compound	iLOGP	XLOGP3	WLOGP	MLOGP	Silicos-IT	Consensus Log $P_{o/w}$
1	3.75	5.65	4.94	2.52	5.1	4.39
2	3.69	5.67	4.9	2.52	5.1	4.38
3	2.61	3.13	2.66	1.13	2.98	2.5
4	2.46	2.18	2.05	1.77	2.26	2.14

Table 4. Water solubility characteristics of the isolated compounds from *C. nodosum*

	ESOL				Ali				Silicos-IT			
	Log S (ESOL)	Solubility		Class	Log S (Ali)	Solubility		Class	Log S Silicos-IT	Solubility		Class
		mg/ml	mol/L			mg/ml	mol/L			mg/ml	mol/L	
1	-5.98	3.93E-04	1.04E-06	MS	-7.09	3.06E-05	8.09E-08	PS	-6.21	2.33E-04	6.15E-07	PS
2	-6	3.82E-04	1.01E-06	MS	-7.11	2.92E-05	7.71E-08	PS	-6.21	2.33E-04	6.15E-07	PS
3	-3.82	3.64E-02	1.50E-04	S	-4.05	2.15E-02	8.87E-05	MS	-4.85	3.45E-03	1.43E-05	MS
4	-2.2	1.34E+00	6.32E-03	S	-2.79	3.44E-01	1.62E-03	S	-2.07	1.79E+00	8.45E-03	S

PS - Poorly soluble; S – Soluble; MS - Moderately soluble

All isolated compounds exhibit high gastrointestinal (GI) absorption based on SwissADME prediction, as shown in Table 5. Notably, compounds **3** and **4** were also predicted to be able to cross the blood-brain barrier (BBB), while compounds **1** and **2** do not. These predictions were consistent with the BOILED-Egg model in Figure 4, which placed compounds **1** and **2** within the GI absorption zone only, while compounds **3** and **4** were within both GI and BBB permeation zones due to their moderate lipophilicity for oral bioavailability and low TPSA value (40 – 60 Å^2), which leads to a good membrane permeability (Möbitz, 2024), giving good permeability even within both zones (Morak-Młodawska et al., 2023). The cytochrome P450 (CYP) enzymes are key mediators of drug metabolism, responsible for the clearance of most xenobiotics, making their inhibition or substrate status a critical determinant of drug-drug interaction risk and metabolic safety (Zanger & Schwab, 2013). In this study, the CYP interaction profiles of all isolated compounds **1**-**4** are tabulated as in Table 5. Compounds **1** and **2** were predicted to inhibit CYP2C19 and CYP2C9, while compound **3** showed broader inhibition of CYP1A2, CYP2D6, and CYP3A4. Such inhibition patterns raise the possibility of drug-drug interactions and reduced metabolic stability (Lee et al., 2024). In contrast, compound **4** exhibited no predicted CYP inhibition, suggesting a safer profile for further pharmacological development (Hakkola et al., 2020).

Table 5. Pharmacokinetic parameters of the isolated compounds from *C. nodosum*

	GI Abs.	BBB permeant	Pgp Sub-strate	CYP1A2 inhibitor	CYP2C19 inhibitor	CYP2C9 inhibitor	CYP2D6 inhibitor	CYP3A4 inhibitor	log Kp (cm/s)
1	High	No	No	No	Yes	Yes	No	No	-4.6
2	High	No	No	No	Yes	Yes	No	No	-4.58
3	High	Yes	No	Yes	No	No	Yes	Yes	-5.56
4	High	Yes	No	No	No	No	No	No	-6.05

From the drug-likeness prediction in Table 6, all compounds satisfied Lipinski's "Rule of Five" (Figure 2) (Ranjith & Ravikumar, 2019), Ghose (Ghose et al., 1998), Veber (Veber et al., 2002), and Egan (Egan et al., 2000) rules, as no violations were observed. This suggests that all the compounds exhibited acceptable oral drug-like properties. However, compounds **1** and **2** violated the Muegge criteria due to their high lipophilicity (XLOGP3 >5) (Muegge et al., 2001), indicating the compounds are too lipophilic, which reduces their aqueous solubility. The medicinal chemistry evaluation in Table 7 further flagged the structural liabilities in compounds **1** and **2,** as both compounds contained two

Brenk alerts due to the presence of the xanthone skeleton structure and an isolated alkene at the C-4 position within the compounds. This indicates that both compounds **1** and **2** are potentially toxic, chemically reactive fragments in the structure of the compounds (Ononamadu & Ibrahim, 2021).

Both compounds also failed lead-likeness in the medicinal chemistry evaluation due to their high molecular weight (> 350 Da) and high lipophilicity (XLOGP > 3.5) (Oprea et al., 2007). A similar situation occurred with compound **3,** as it showed one Brenk alert for its polycyclic aromatic hydrocarbon in its xanthone skeleton and failed lead-likeness due to low molecular weight (< 250 Da). On the other hand, compound **4** carried no PAINS or Brenk alerts, except for failing the lead-likeness only due to its low molecular weight (< 250 Da). The synthetic accessibility scores in Table 7 indicated that all compounds were within a feasible range for chemical synthesis (Ertl & Schuffenhauer, 2009).

The bioavailability radar plots in Figure 3 provided an integrated view of oral drug-likeness, as all compounds fit within the optimal physicochemical ranges, with compounds **1** and **2** approaching the lipophilicity threshold, resulting in their reduced solubility. Meanwhile, compounds **3** and **4** displayed more balanced radar profiles, falling within both GI absorption and BBB zones, suggesting a better opportunity for future development.

Table 6. Drug-likeness rule and bioavailability score of the isolated compounds from *C. nodosum*

Compound	Lipinski	Ghose	Veber	Egan	Muegge	Bioavailability score
1	0	0	0	0	1; XLOGP3 > 5	0.55
2	0	0	0	0	1; XLOGP3 > 5	0.55
3	0	0	0	0	0	0.55
4	0	0	0	0	0	0.55

0 = no violation; 1 = has violation

Table 7. Medicinal properties of the isolated compounds from *C. nodosum*

Compound	Pains	Brenk	Leadlikeness	Synthetic accessibility
1	0	2 alerts on the molecular structures: (a) isolated alkene (b) polycyclic aromatic hydrocarbon	N, 2 violations: (a) MW > 350 (b) XLOGP3 > 3.5	4.13
2	0	2 alerts on the molecular structures: (a) isolated alkene (b) polycyclic aromatic hydrocarbon	N, 2 violations: (a) MW > 350 (b) XLOGP3 > 3.5	4.11
3	0	1 alert on the molecular structures: (a) polycyclic aromatic hydrocarbon	N, 1 violation: (a) MW < 250	2.8
4	0	0	N; 1 violation: (a) MW < 250	3.59

0 = no alert, N = No, Pains = Pan-Assay INterference compoundS, structural motifs prone to false-positive bioassay results, Brenk = Filters identifying potentially toxic, unstable, or chemically problematic fragments

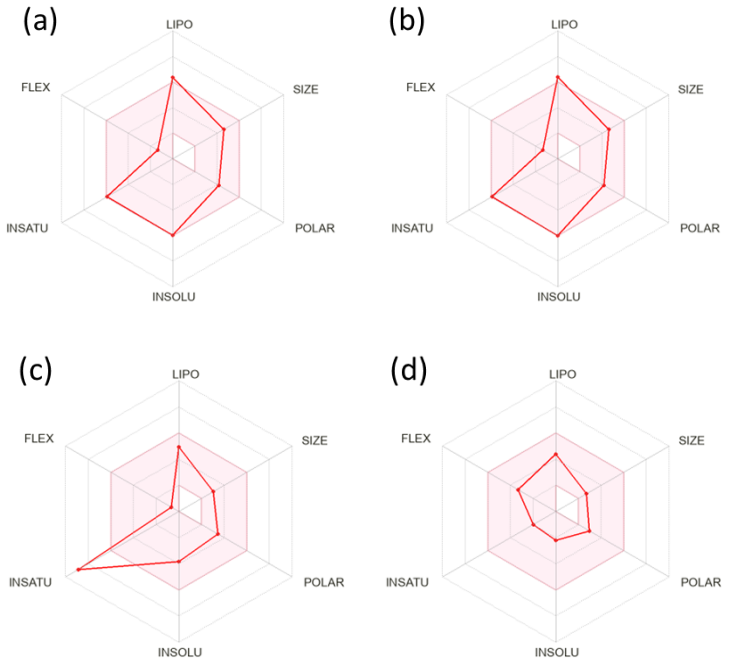

Figure 3. The bioavailability radar view of all isolated compounds **1**-**4**. The pink area represents the optimal range for each property of LIPO = lipophilicity, SIZE = size of molecular weight, POLAR = polarity, INSOLU = insolubility, INSATU = insaturation, FLEX = flexibility; (a) Radar view of (**1**); (b) Radar view of (**2**); (c) Radar view of (**3**); (d) Radar view of (**4**)

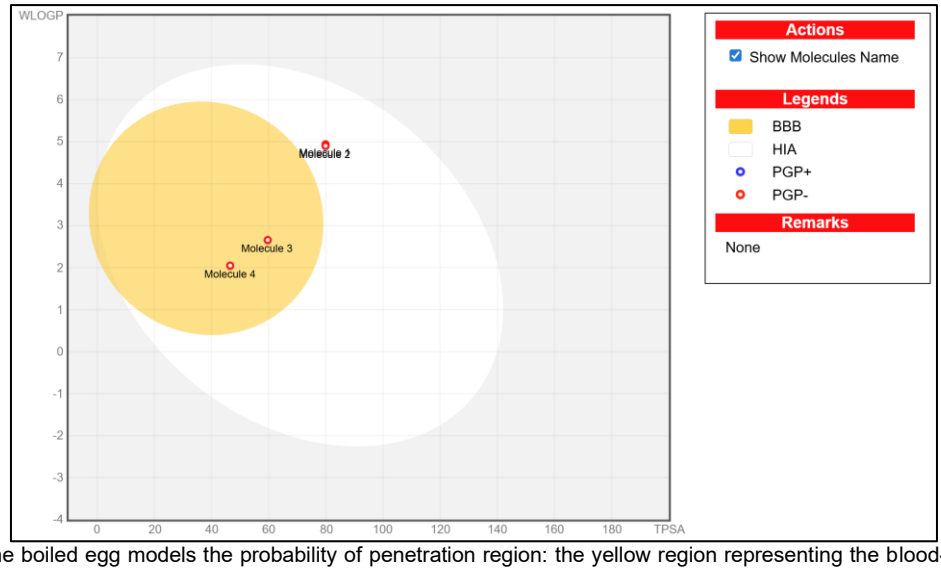

Figure 4. The boiled egg models the probability of penetration region: the yellow region representing the blood-brain barrier, the white region representing the gastrointestinal tract and the red points represent molecules not actively effluxed by P-glycoprotein (P-gp)

3.3.2. pkCSM for ADME/Tox Predictions

Following the initial pharmacokinetic assessment using SwissADME, the pkCSM platform was employed to cross-validate key ADME and toxicity endpoints of all compounds **1**-**4**. The predictions generated by pkCSM largely supported the SwissADME results, particularly in relation to absorption and distribution parameters, while providing additional insights into transporter interactions, clearance, and toxicity profiles (Yeni & Rachmania, 2022). All parameters are interpreted following the theory and guidelines given by Pires et al. (2015). Consistent with SwissADME, all compounds exhibited high intestinal absorption (>92%), with compounds **1** (95.5%) and **2** (92.3%) showing less efficient BBB penetration (log BB = –0.249 and –0.269, respectively) when compared to compounds **3** (95.2%) and **4** (94.9%), which have better BBB penetration (log BB = -0.028 and -0.108, respectively). This explains that the red points of compounds **3** and **4** were observed at the BBB zones, but not compounds **1** and **2**, as shown in Figure 4. The CNS penetration shows compounds **1** and **2** were predicted to have low CNS permeability (log PS = -1.752 and -1.672, respectively), while compound **3** was borderline poor (log PS = -2.024), and compound **4** has poor CNS penetration (log PS = -2.798). However, pkCSM further identified compounds **1**-**3** as P-glycoprotein (P-gp) substrates, with compounds **1** and **2** also acting as P-gp I and II inhibitors, highlighting a potential risk for efflux-mediated drug resistance that is not captured in SwissADME (Lagares et al., 2019). The metabolism profiles showed strong agreement with Swiss ADME regarding cytochrome P450 interactions, as the pkCSM tool refined these predictions by specifying the substrate status. Compounds **1** and **2** were both predicted to be CYP3A4 substrates and inhibitors of CYP1A2, CYP2C19, and CYP2C9, in line with SwissADME. Compound **3** was also predicted as a CYP3A4 substrate with inhibitory activity against CYP1A2 and CYP2C19, while compound **4** showed no significant CYP inhibition or substrate properties, reinforcing the prediction of its safer metabolic profile in SwissADME (Hakkola et al., 2020).

A key area where pkCSM extended SwissADME was in the clearance and toxicity evaluation, whereby compound **4** displayed the highest predicted clearance (log CL = 1.528), suggesting lower systemic accumulation, while compounds **1**, **2**, and **3** showed lower clearance values (log CL = 0.087, 0.197, and 0.151, respectively). Toxicity predictions are the part that distinguishes compounds **1** and **2**, as compound **1** was Ames-negative, non-hepatotoxic, and tolerated at higher doses (log mg/kg/day = 0.22), while compound **2** was Ames-positive, hepatotoxic, predicted to have a lower maximum tolerated dose (log mg/kg/day = -0.037) and have higher chronic toxicity (LOAEL = 1.392). Compounds **3** and **4** both exhibited relatively safer profiles, although compound **3** was flagged as Ames-positive, and compound **4** as a potential skin sensitiser. Notably, hERG inhibition risks were minimal across all compounds, with only compounds **1** and **2** showing weak hERG II inhibition. Importantly, the pkCSM supported the SwissADME prediction with additional mechanistic details that helped differentiate the two structurally related compounds. Despite the identical physicochemical profiles, compounds **1** and **2** differ in predicted genotoxicity and hepatotoxicity. While compounds **3** and **4** emerged as comparatively safer, compound **4** demonstrated the most favourable combination of solubility, clearance, and lack of major CYP liabilities. Table 8 shows the results of the ADMET test with pkCSM of all the isolated compounds.

Table 8. The results of the ADMET prediction parameters using pkCSM on compounds **1-4**

Parameters		1	2	3	4
A					
Water solubility (log mol/L)		-4.318	-5.155	-3.868	-1.737
Caco-2 permeability (log Papp)		0.811	0.723	1.187	1.325
Intestinal absorption (%)		95.458	92.286	95.21	94.877
Skin permeability (log Kp)		-2.737	-2.932	-2.753	-2.809
P-gp substrate		Y	Y	Y	N
P-gp I inhibitor		Y	Y	N	N
P-gp II inhibitor		Y	Y	Y	N
D					
VDss (log L/kg)		0.297	0.274	-0.048	-0.043
Fraction unbound (Fu)		0	0.031	0.09	0.489
BBB permeability (log BB)		-0.249	-0.269	-0.028	-0.108
CNS permeability (log PS)		-1.752	-1.672	-2.024	-2.798
M					
Substrate	CYP2D6	N	N	N	N
	CYP3A4	Y	Y	Y	N
Inhibitor	CYP1A2	Y	Y	Y	N
	CYP2C19	Y	Y	Y	N
	CYP2C9	Y	Y	N	N
	CYP2D6	N	N	N	N
	CYP3A4	N	Y	N	N
E					
Total clearance (log mL/min/kg)		0.087	0.197	0.151	1.528
Renal OCT2 substrate		N	N	N	N
T					
AMES toxicity		N	Y	Y	N
Max tolerated dose (log mg/kg/day)		0.22	-0.037	0.078	0.595
hERG I inhibition (cardiotoxicity)		N	N	N	N
hERG II inhibition (cardiotoxicity)		Y	Y	N	N
Oral rat acute toxicity (LD50, mol/kg)		1.887	2.007	1.777	1.882
Oral rat chronic toxicity (LOAEL, log mg/kg/day)		0.52	1.392	0.965	2.54
Hepatotoxicity		N	Y	N	N
Skin sensitisation		N	N	N	Y
T. pyriformis toxicity (log ug/L)		0.428	0.607	0.986	0.471
Minnow toxicity (log mM)		-0.334	-0.634	0.235	1.573

A = Absorption; D = Distribution; E = Excretion; M = Metabolism; T = Toxicity; Y = Yes; N = No

3.4. Molecular Docking

Nucleic acid synthesis inhibition is one of the targeted strategies by interfering with the antibacterial mechanism and thus reducing bacterial proliferation (Heilman et al., 2023). The nucleic acid synthesis inhibition could be done through the inhibition of the topoisomerase enzyme, such as DNA gyrase. These enzymes are essential for bacterial growth (Farhadi et al., 2019) and function to relax supercoiled DNA in the DNA replication process (Collin et al., 2011). DNA gyrase retains active sites that are susceptible to small molecule inhibitors such as coumarins and quinolones. These similarities suggest that designing small-molecule inhibitors targeting these active sites would be a promising strategy to inhibit the DNA gyrase, thereby enhancing the antibacterial efficacy (Bellon et al., 2004). The in-silico screening procedure was performed to identify the possible mechanism of action of the isolated compounds in the antibacterial activities at the molecular level and determine the potential DNA gyrase inhibitors.

A redocking procedure was performed using the DNA gyrase enzyme (PDB ID: 5L3J) complexed with its co-crystallised ligand, BDBM50198240, to ensure the reliability and reproducibility of the initial protocol used. The docking parameters were validated by comparing the binding orientation of the redocked ligand with that of the original co-crystallised ligand. As illustrated in Figure 5, the best docking pose of the redocked ligand was superimposed onto the native ligand within the active site of the enzyme. The root-mean-square deviation (RMSD) between the two conformations was calculated to assess the accuracy of the docking protocol. An RMSD value of 0.7774 Å was obtained, which is well below the accepted threshold of 3.0 Å, indicating a high level of agreement between the predicted and experimental binding modes. The RMSD value of less than 3Å is considered valid and will be accepted in this study, as it reveals the accuracy of the docking protocols in reproducing the initial crystal structures (Zaine et al., 2024).

The molecular docking study reveals that compound **1** gives the highest binding energy with -7.9 Kcal/mol compared to other isolated compounds and BDBM50198240 (Table 9). Figure 5 shows the alignment of trapezifolixanthone (**1**) in DNA gyrase binding pockets and their 2D ligand-receptor interaction. Trapezifolixanthone (**1**) forms two hydrogen bonds with ASN46 and THR165. Most of the

hydrogen bonds were developed between hydroxy substituents. The observed high binding affinity and target specificity are closely linked to the limited number of hydrogen bonds formed between the ligand and the therapeutic target (Patil et al., 2010). Besides, trapezifolixanthone (**1**) possesses similar binding modes with clorobiocin, a DNA gyrase inhibitor measured by X-ray crystallography. The similar amino acids are ASP 73, ALA 47, and VAL 120 (Brvar et al., 2012). Compound **1** also interacted with other amino acids, such as VAL167, VAL43, VAL120, GLU50, GLY77, ILE94, and PRO79 through Van der Waals, pi-sigma, and pi-alkyl. Meanwhile, caloxanthone C (**2**) forms two hydrogen bonds with the amino acids GLY77 and GLU50, along with van der Waals interactions involving ASN46 and THR165. Compound **3** exhibits a single hydrogen bond with ASN46, similar to Trapifolixanthone (**1**). Besides, compounds **3** shows π-alkyl and van der Waals interactions with residues ALA47, VAL120, and ASP73 similar to the interaction profile of Clorobiocin (Brvar et al., 2012). In contrast, canumolactone (**4**) does not form any hydrogen bonds, resulting in weaker binding interactions compared to the other isolated compounds.

Table 9. Binding Energy for isolated compounds from *C. nodosum* and redocking co-crystallised ligand against DNA gyrase

Compounds	Binding energy (kcal/mol)
1	-7.9
2	-7.6
3	-7.6
4	-6.2
BDBM50198240	-7.5

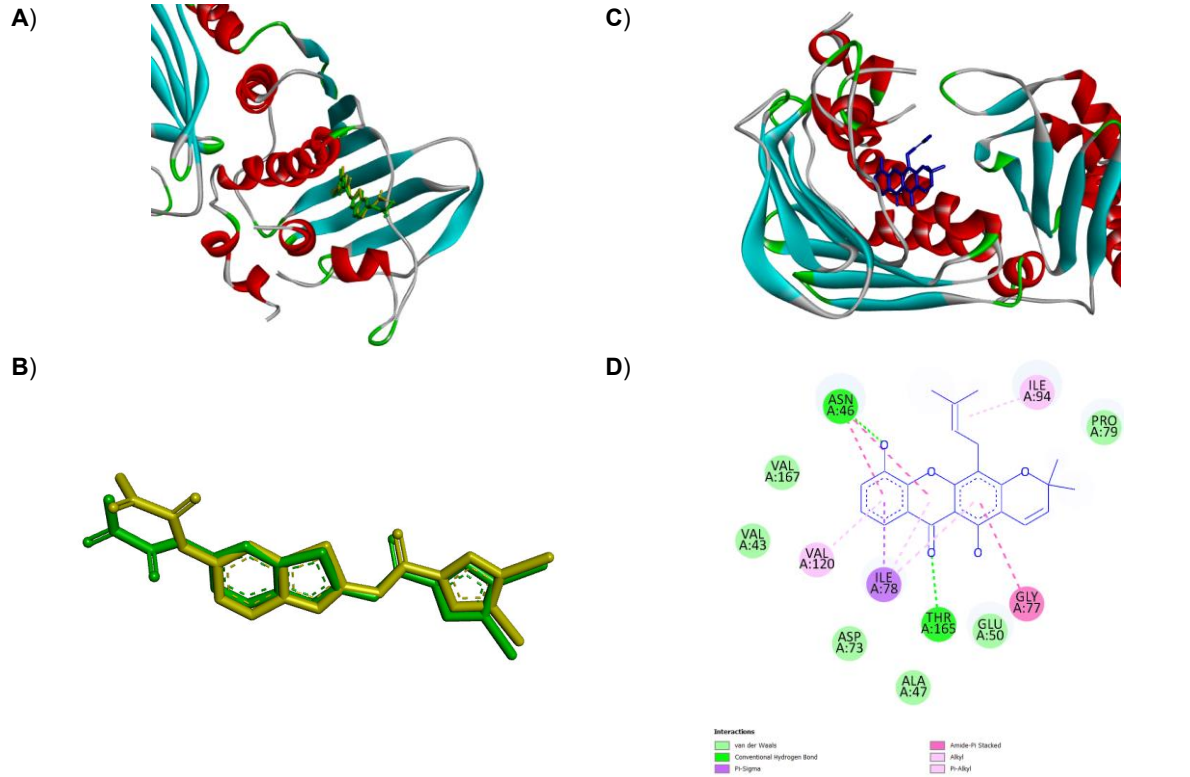

Figure 5. (**A**) alignment of the redocked BDBM50198240 (green model) and BDBM50198240 co-crystallized (yellow model) in the binding site of DNA gyrase enzyme; (**B**) superimposition of the redocked BDBM50198240 (green model) and BDBM50198240 crystal (yellow model); (**C**) Trapezifolixanthone (**1**) (blue model) in the binding site of DNA gyrase; (**D**) the 2D schematic residues within the binding site of DNA gyrase that exhibits hydrogen bonding and hydrophobic interaction with trapezifolixanthone (**1**)

4. CONCLUSION

In this study, four secondary metabolites, namely trapezifolixanthone (**1**), caloxanthone C (**2**), 1-hydroxy-7-methoxyxanthone (**3**), and canumolactone (**4**), were successfully isolated and structurally characterised from the stem bark of *C. nodosum* and structurally characterised. In silico ADME/Tox predictions using SwissADME and pkCSM revealed that all compounds met Lipinski's Rule of Five and displayed favourable pharmacokinetic features, with canumolactone (**4**) emerging as the most promising due to its solubility, clearance, and lack of major CYP liabilities. The molecular docking also highlighted that trapezifolixanthone (**1**) is the most potent DNA gyrase binder, suggesting its potential

as a lead scaffold. Overall, the combined computational analyses provide preliminary support for the antibacterial potential of *C. nodosum* metabolites, warranting further in vitro and in vivo validation.

ACKNOWLEDGEMENT
The authors gratefully acknowledge the Ministry of Higher Education, Malaysia, for the Fundamental Research Grant Scheme (FRGS) funds [FRGS/1/2023/STG01/UNIMAS/03/5], Universiti Malaysia Sarawak (UNIMAS), and Universiti Teknologi MARA (UiTM) for providing research facilities and the Sarawak Biodiversity Centre (SBC).

CONFLICT OF INTEREST
The authors declare no conflicts of interest.

AUTHOR CONTRIBUTION
Yiizamy Suffian: Writing original draft, visualisation, investigation, methodology, and data curation. Vivien Jong Yi Mian: Conceptualisation, methodology, validation, resources, supervision, and project administration. Nor Hisam Zamakshshari: Writing, review, editing, conceptualisation, methodology, validation, resources, supervision, and project administration. Ainaa Nadiah Abd Halim: Writing, review, editing, conceptualisation, and project administration. Jiumn-Yih Wu, Wafa M. Al Madhagi: Writing, review, editing, and conceptualisation.

DATA AVAILABILITY
The authors confirm that the data supporting the findings of this study are available within the article.

DECLARATION OF GENERATIVE AI
During the preparation of this work, the author used ChatGPT in order to assist in drafting the abstract. After using the tool, the author reviewed and edited the content as needed to improve the sentence and grammar of the manuscript. The authors also take full responsibility for the content of the publication.

ETHICS
Not applicable.

REFERENCES

Al Azzam KM. (2023). SwissADME and pkCSM webservers predictors: an integrated online platform for accurate and comprehensive predictions for in silico ADME/T properties of artemisinin and its derivatives. *Kompleksnoe Ispolzovanie Mineralnogo Syra*, 325(2), 14-21. doi:10.31643/2023/6445.13

Bellon S, Parsons JD, Wei Y, Hayakawa K, Swenson LL, Charifson PS, Lippke JA, Aldape R, Gross CH. (2004). Crystal structures of *Escherichia coli* topoisomerase IV ParE subunit (24 and 43 Kilodaltons): a single residue dictates differences in novobiocin potency against topoisomerase IV and DNA gyrase. *Antimicrobial Agents and Chemotherapy*, 48(5), 1856-1864. doi:10.1128/AAC.48.5.1856-1864.2004

Chinthu RV, Raveendran PB, Raveendran M. (2023). A review on the genus *Calophyllum* (Clusiaceae): a potential medicinal tree species. *Plant Science Today*, 10(3), 1-5. doi:10.14719/PST.1818

Collin F, Karkare S, Maxwell A. (2011). Exploiting bacterial DNA gyrase as a drug target: Current state and perspectives. *Applied Microbiology and Biotechnology*, 92(3), 479-497. doi:10.1007/S00253-011-3557-Z/FIGURES/7

Daina A, Michielin O, Zoete V. (2017). SwissADME: A free web tool to evaluate pharmacokinetics, drug-likeness and medicinal chemistry friendliness of small molecules. *Scientific Reports*, 7, 42717. doi:10.1038/SREP42717

Dharmaratne HRW, Napagoda MT, Tennakoon SB. (2009). Xanthones from roots of *Calophyllum thwaitesii* and their bioactivity. *Natural Product Research*, 23(6), 539-545. doi:10.1080/14786410600899118

Eberhardt J, Santos-Martins D, Tillack AF, Forli S. (2021). AutoDock Vina 1.2.0: New docking methods, expanded force field, and python bindings. *Journal of Chemical Information and Modeling*, 61(8), 3891-3898. doi:10.1021/ACS.JCIM.1C00203

Egan WJ, Merz KM, Baldwin JJ. (2000). Prediction of drug absorption using multivariate statistics. *Journal of Medicinal Chemistry*, 43(21), 3867-3877. doi:10.1021/JM000292E

Ertl P, Schuffenhauer A. (2009). Estimation of synthetic accessibility score of drug-like molecules based on molecular complexity and fragment contributions. *Journal of Cheminformatics*, 1, 1-11. doi:10.1186/1758-2946-1-8/TABLES/1

Farhadi F, Khameneh B, Iranshahi M, Iranshahy M. (2019). Antibacterial activity of flavonoids and their structure-activity relationship: An update review. *Phytotherapy Research*, 33(1), 13-40. doi:10.1002/PTR.6208

Farida, S., Jenie, R. I., & Fakhrudin, N. (2024). Calophyllum inophyllum: A Comprehensive Analysis of its Ethnobotanical, Phytochemical, and Pharmacological Properties. *Majalah Obat Tradisional*, *29*(2), 121–142. doi:10.22146/mot.87488

Feng Z, Lu X, Gan L, Zhang Q, Lin L. (2020). Xanthones a promising anti-inflammatory scaffold: structure, activity, and drug likeness analysis. *Molecules*, 25(3), 598. doi:10.3390/MOLECULES25030598

Ghose AK, Viswanadhan VN, Wendoloski JJ. (1998). A knowledge-based approach in designing combinatorial or medicinal chemistry libraries for drug discovery: A qualitative and quantitative characterization of known drug databases. *Journal of Combinatorial Chemistry*, 1(1), 55-68. doi:10.1021/CC9800071

Glanzmann N, de Oliveira Lemos AS, Meinel RS, Torres Branca M, Mayrink NS, Da Costa Nunes IK, Pereira H, MG, Coimbra ES, Fabri RL, da Silva AD. (2024). New quinoline derivatives and their antimicrobial potential against *Candida albicans* and *Staphylococcus aureus*. *ChemistrySelect*, 9(36), e202401828. doi:10.1002/SLCT.202401828

Hakkola J, Hukkanen J, Turpeinen M, Pelkonen O. (2020). Inhibition and induction of CYP enzymes in humans: an update. *Archives of Toxicology*, *94*(11), 3671-3722. doi:10.1007/S00204-020-02936-7/TABLES/14

Hanwell MD, Curtis DE, Lonie DC, Vandermeerschd T, Zurek E, Hutchison GR. (2012). Avogadro: An advanced semantic chemical editor, visualization, and analysis platform. *Journal of Cheminformatics*, 4(8), 1-17. doi:10.1186/1758-2946-4-17/FIGURES/14

Heilman DNAA, Hui AYC, Jong VYM, Ahmad FB, Cee LP, Stanslas J, Zamakshshari NH. (2023). Unlocking the antibacterial potential of xanthone from *Calophyllum* species: Inhibition of nucleic acid synthesis. *ChemistrySelect*, 8(46), e202302737. doi:10.1002/SLCT.202302737

Hong Z, Yu TT, Yasir M, Sara M, Black DSC, Willcox MDP, Kuppusamy R, Kumar N. (2024). Daidzein-based amphiphilic small molecular antimicrobial peptidomimetics as novel antimicrobial agents with anti-Biofilm activity. *ChemistrySelect*, 9(22), e202400502. doi:10.1002/SLCT.202400502

Karunakaran T, Firouz NS, Santhanam R, Jong VYM. (2022). Phytochemicals from *Calophyllum macrocarpum* Hook.f. and its cytotoxic activities. *Natural Product Research*, 36(2), 654-659. doi:10.1080/14786419.2020.1795658

Kurniawan YS, Priyangga KTA, Jumina, Pranowo HD, Sholikhah EN, Zulkarnain AK, Fatimi HA, Julianus J. (2021). An update on the anticancer activity of xanthone derivatives: a review. *Pharmaceuticals*, 14(11), 1144. doi:10.3390/PH14111144

Lagares LM, Minovski N, Novič M. (2019). Multiclass classifier for P-glycoprotein substrates, inhibitors, and non-active compounds. *Molecules*, 24(10), 2006. doi:10.3390/MOLECULES24102006

Lee J, Beers JL, Geffert RM, Jackson KD. (2024). A review of CYP-mediated drug interactions: mechanisms and in vitro drug-drug interaction assessment. *Biomolecules*, 14(1), 99. doi:10.3390/BIOM14010099

Leslie Gunatilaka AA, Jasmin De Silva AMY, Sotheeswaran S. (1982). Minor xanthones of *Hypericum* mysorense. *Phytochemistry*, 21(7), 1751-1753. doi:10.1016/S0031-9422(82)85053-X

Li Z, Chen K, Rose P, Zhu YZ. (2022). Natural products in drug discovery and development: Synthesis and medicinal perspective of leonurine. *Frontiers in Chemistry*, 10, 1036329. doi:10.3389/FCHEM.2022.1036329/BIBTEX

Lizazman MA, Jong VYM. (2024). Antioxidant potential of *Calophyllum canum* P.F. Stevens: Xanthones, phenolics, and radical scavenging activity. [Preprint], Universiti Teknologi MARA. doi:10.21203/RS.3.RS-4336474/V1

Lizazman MA, Jong VYM, Chua PF, Lim WK, Karunakaran T. (2023). Phytochemicals from *Calophyllum canum* Hook f. ex T. Anderson and their neuroprotective effects. *Natural Product Research*, 37(12), 2043-2048. doi:10.1080/14786419.2022.2116021

Möbitz H. (2024). Design principles for balancing lipophilicity and permeability in beyond rule of 5 Space. *ChemMedChem*, 19(5), e202300395. doi:10.1002/CMDC.202300395

Morak-Młodawska B, Jeleń M, Martula E, Korlacki R. (2023). Study of lipophilicity and ADME properties of 1,9-diazaphenothiazines with anticancer action. *International Journal of Molecular Sciences*, 24(8), 6970. doi:10.3390/IJMS24086970

Morris GM, Ruth H, Lindstrom W, Sanne MF, Belew RK, Goodsell DS, Olson AJ. (2009). Software news and updates AutoDock4 and AutoDockTools4: Automated docking with selective receptor flexibility. *Journal of Computational Chemistry*, 30(16), 2785-2791. doi:10.1002/JCC.21256

Muegge I, Heald SL, Brittelli D. (2001). Simple selection criteria for drug-like chemical matter. *Journal of Medicinal Chemistry*, 44(12), 1841-1846. doi:10.1021/JM015507E

Murray CJL, Ikuta KS, Sharara F, Swetschinski L, Robles AG, Gray A, Han C, Bisignano C, Rao P, Wool E, Johnson SC, Browne AJ, Chipeta MG, Fell F, Hackett S, Haines-Woodhouse G, Kashef Hamadani BH, Kumaran EAP, McManigal B, Agarwal R, Akech S, Albertson S, Amuasi J, Andrews J, Aravkin A, Ashley E, Bailey F, Baker S, Basnyat B, Bekker A, Bender R, Bethou A, Bielicki J, Boonkasidecha S, Bukosia J, Naghavi M.(2022). Global burden of bacterial antimicrobial resistance in 2019: a systematic analysis. *The Lancet*, 399(10325), 629-655. doi.org/10.1016/S0140-6736(21)02724-0

Newman DJ, Cragg GM. (2020). Natural products as sources of new drugs over the nearly four decades from 01/1981 to 09/2019. *Journal of Natural Products*, 83(3), 770-803. doi:10.1021/acs.jnatprod.9b01285

Ononamadu CJ, Ibrahim A. (2021). Molecular docking and prediction of ADME/drug-likeness properties of potentially active antidiabetic compounds isolated from aqueous-methanol extracts of *Gymnema sylvestre* and *Combretum micranthum*. *BioTechnologia*, 102(1), 85. doi:10.5114/BTA.2021.103765

Oprea TI, Allu TK, Fara DC, Rad RF, Ostopovici L, Bologa CG. (2007). Lead-like, drug-like or "Pub-like": How different are they?. *Journal of Computer-Aided Molecular Design*, 21, 113-119. doi:10.1007/S10822-007-9105-3/TABLES/4

Pinto MMM, Palmeira A, Fernandes C, Resende DISP, Sousa E, Cidade H, Tiritan ME, Correia-Da-silva M, Cravo S. (2021). From natural products to new synthetic small molecules: A journey through the world of xanthones. *Molecules*, 26(2), 431. doi:10.3390/MOLECULES26020431

Pires DEV, Blundell TL, Ascher DB. (2015). pkCSM: Predicting Small-Molecule Pharmacokinetic and Toxicity Properties Using Graph-Based Signatures. *Journal of Medicinal Chemistry*, 58(9), 4066-4072. doi:10.1021/ACS.JMEDCHEM.5B00104

Rai M, Singh AV, Paudel N, Kanase A, Falletta E, Kerkar P, Heyda J, Barghash RF, Pratap Singh S, Soos M. (2023). Herbal concoction unveiled: A computational analysis of phytochemicals' pharmacokinetic and toxicological profiles using novel approach methodologies (NAMs). *Current Research in Toxicology*, 5, 100118. doi:10.1016/J.CRTOX.2023.100118

Ranjith D, Ravikumar C. (2019). SwissADME predictions of pharmacokinetics and drug-likeness properties of small molecules present in Ipomoea mauritiana Jacq. *Journal of Pharmacognosy and Phytochemistry*, 8(5), 2063-2073.

Remali J, Sahidin I, Aizat WM. (2022). Xanthone biosynthetic pathway in plants: a review. *Frontiers in Plant Science*, 13, 809497. doi:10.3389/FPLS.2022.809497/BIBTEX

Salam MA, Al-Amin MY, Salam MT, Pawar JS, Akhter N, Rabaan AA, Alqumber MAA. (2023). Antimicrobial resistance: a growing serious threat for global public health. *Healthcare*, 11(13), 1946. doi:10.3390/HEALTHCARE11131946

Trott O, Olson AJ. (2010). AutoDock Vina: Improving the speed and accuracy of docking with a new scoring function, efficient optimization, and multithreading. *Journal of Computational Chemistry*, 31(2), 455-461. doi:10.1002/JCC.21334

Veber DF, Johnson SR, Cheng HY, Smith BR, Ward KW, Kopple KD. (2002). Molecular properties that influence the oral bioavailability of drug candidates. *Journal of Medicinal Chemistry*, 45(12), 2615-2623. doi:10.1021/JM020017N

Wei W, Cherukupalli S, Jing L, Liu X, Zhan P. (2020). Fsp3: A new parameter for drug-likeness. *Drug Discovery Today*, 25(10), 1839-1845. doi:10.1016/J.DRUDIS.2020.07.017

Xiong G, Wu Z, Yi J, Fu L, Yang Z, Hsieh C, Yin M, Zeng X, Wu C, Lu A, Chen X, Hou T, Cao D. (2021). ADMETlab 2.0: An integrated online platform for accurate and comprehensive predictions of ADMET properties. *Nucleic Acids Research*, 49(1), 5-14. doi:10.1093/NAR/GKAB255

Yeni Y, Rachmania RA. (2022). The prediction of pharmacokinetic properties of compounds in *Hemigraphis alternata* (Burm.F.) T. Ander leaves using pkCSM. *Indonesian Journal of Chemistry*, 22(4), 1081-1089. doi:10.22146/IJC.73117

Zailan AAD, Karunakaran T, Abu Bakar MH, Jong VYM. (2022). The Malaysian genus *Calophyllum* (Calophyllaceae): a review on its phytochemistry and pharmacological activities. *Natural Product Research*, 36(17), 4575-4585. doi:10.1080/14786419.2021.1982936

Zaine NFZ, Halim ANA, Saat R, Jong VYM, Zamakshshari NH. (2024). Antibacterial activity of *Garcinia* spp. by molecular docking simulations: An overview. *Phytochemistry Reviews*, 24, 587-2628. doi:10.1007/s11101-024-09997-x

Zaini NNM, Salleh WMNHW, Salihu AS, Sungthong B. (2025). Unlocking the potential of *Calophyllum* xanthones: A review on antileukemic activity and molecular docking insights. *Journal of Science and Mathematics Letters*, 13(1), 168-186. doi:10.37134/jsml.vol13.1.15.2025

Zamakshshari NH, Ee GCL, Teh SS, Daud S, Karunakaran T, Safinar I. (2016). Natural product compounds from *Calophyllum depressinervosum*. *Pertanika Journal of Tropical Agricultural Science*, 39(2), 249-255.

Zanger UM, Schwab M. (2013). Cytochrome P450 enzymes in drug metabolism: Regulation of gene expression, enzyme activities, and impact of genetic variation. *Pharmacology & Therapeutics*, 138(1), 103-141. doi:10.1016/J.PHARMTHERA.2012.12.007